Opt Quant Electron (2018) 50:69
https://doi.org/10.1007/s11082-018-1344-0

Confined optical beam-bending for direct connection among cores of different multicore fibers

Ehab Awad[1]

Received: 14 August 2017 / Accepted: 18 January 2018 / Published online: 22 January 2018

Abstract In future multicore optical fibers (MCFs) networks, it is crucial to have optical devices which can manipulate propagating signals directly without conversion back and forth to single-core optical fibers. That is because these conversions may degrade such networks potential high-capacity. In this work, a 90° silica-glass confined beam-bending (CBB) device with a bending-radius of 160 μm is numerically demonstrated. The CBB design and material allow for direct space-division connections among single-mode cores of different multi-core and/or single-core fibers without a need for special spot-size converters or mode tapers. The CBB can be cascaded to maneuver propagating beams around sharp corners in three-dimensional space in order to obtain flexible connections within small areas. A simple example of universal multicore connector between different optical fibers is also numerically demonstrated. The simulations show wideband operation over the S, C, L, and U wavelength range with small insertion-loss, polarization-dependent loss, in addition to reasonable return-loss and crosstalk. It also shows cascadability and good tolerance to MCFs core variations, in addition to CBB design parameters.

Keywords Optical fiber communication · Multicore optical fibers · Optical fiber components

1 Introduction

Space-division-multiplexing (SDM) in optical multicore fibers (MCFs) is considered one of the key solutions to increase capacity in future optical fiber communication networks. In MCF, each core can carry same set of time-division-multiplexed, dense-wavelength-division-multiplexed, and polarization-division-multiplexed data, in addition to various

✉ Ehab Awad
esawad@ieee.org

[1] Electrical Engineering Department, College of Engineering, King Saud University, Riyadh 11421, Saudi Arabia

complex modulation formats. Therefore, the network capacity can be multiplied (Essiambre et al. 2010, 2013; Zhu et al. 2012; Richardson et al. 2013; Chralyvy 2009). Nowadays, MCFs applications are expanding from optical communications to optical sensing, astronomy, and chip-to-chip interconnects (Kaminow et al. 2013). However in order to avoid sacrificing such potential high capacity in future MCF networks, new optical signal processing devices such as couplers, interconnects, multiplexers, routers, switches, etc. are required to manipulate propagating data signals directly on MCFs without conversion back and forth to single-core single-mode fibers (SMFs) (Awad 2015a, b). These SMFs conversions are considered the main bottleneck that can hinder such capacity increase. In addition, the required components for such conversions are usually bulky, expensive, and complex to deploy within MCFs networks. Therefore having compatible devices that can be connected directly or integrated within MCFs to directly perform such signal processing operations can preserve and fully exploit the high potential capacity of future MCFs networks. One of these MCF devices are optical space division connectors that can simply and directly connect between various types of MCFs cores and/or single-core SMFs in order to redistribute and re-route propagating data signals.

Different techniques have been reported on connections or conversions from MCFs to SMFs. For example, free-space bulk lenses were utilized to collimate and focus SMFs output beams onto 19-cores MCF (Klaus et al. 2012). A tapered multicore connector (TMC) consisting of seven SMFs was fusion spliced to 7-core MCF (Zhu et al. 2010, 2012). Also, photonic-lanterns with adiabatic gradual tapered waveguides were utilized to focus beams on MCF cores (Essiambre et al. 2013; Leon-Saval et al. 2010). In addition, ultrafast laser inscription has been utilized to fabricate three dimensional waveguides fan-out device for coupling several SMFs to a single MCF (Thomson et al. 2007, 2012). However, all such techniques are concerned only with connections to SMFs and the connections bends are usually gradual without sharp 90° bends that can maneuver around tight corners. Nevertheless, to the best of my knowledge, none of these techniques has reported on direct connections between different MCFs.

Moreover, other applications have been reported in literature that are concerned with sharp beam bending. For example, micro and nano fibers with high-index contrast has shown sharp beam bends with a radius as low as $\cong$ 10 μm (Li and Tong 2008). However, the high-index contrast fibers mandates very small core diameters in order to keep single-mode operation. Subsequently, it is unavoidable to use spot-size converters and/or mode tapers to connect micro/nano fibers with standard size optical fibers. Also, standard photonic crystals fibers have demonstrated sharp beam bends with a radius $\cong$ 200 μm and bending loss $\cong$ 10^3 dB/m (Wijeratne et al. 2012). However, the photonics crystal fibers is difficult to be directly fusion spliced with standard optical fibers, and it also suffer from wavelength dependent connection misalignments. In Popovic et al. (2002), a high index-contrast silica waveguide was achieved by utilizing air trenches. Therefore, sharp beam bends having a radius of 20 μm could be achieved with the aid of cladding tapers. However, all these reported sharp beam bends techniques were not originally designed for multi-core optical fiber connections where a direct core-to-core connection is required and bends could be oriented in any direction within the three-dimensional (3D) space.

In this work, a novel confined beam bending (CBB) device using simple total-internal reflection (TIR) phenomenon inside tilted graded-index waveguides is numerically demonstrated by finite-difference-time-domain (FDTD) method. The CBB device can directly connect on core-to-core basis between different MCFs and/or SMFs. The device is designed using silica-glass material which is compatible with most standard optical fibers and thus can allow for fusion spliced or butt-coupled connection. Also, preserving a

confined beam bending shape ensures a single-mode matching between input and output cores without a need for intermediate spot-size converters and/or mode tapers. In addition, the small 90° bending radius of 160 μm allows to maneuver around sharp corners and thus achieving small routing areas. Moreover, the CBB device can be oriented in any direction within the 3D space to achieve universal multicore connections among different types of MCFs and/or SMFs. The CBB device together with some illustrated bendings configurations in addition to a simple example of universal multicore connector (UMC) are characterized and evaluated here by numerical simulations. The CBB and UMC show good performance characteristics that are considered attractive for next generation high capacity MCF optical networks. To the best of my knowledge, this is a new 90° graded-index CBB device, which can connect directly among different single-mode fibers (either single or multi core). Also, it is the first time to report on a universal space-division multicore connector for direct connection and cores redistribution among different MCFs and/or SMFs.

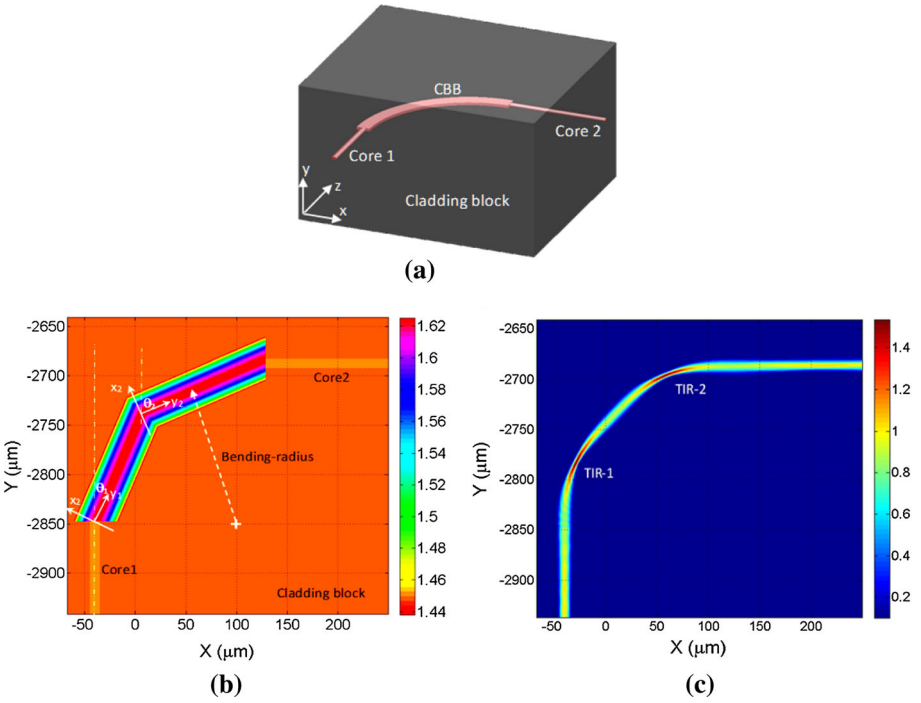

Fig. 1 The confined beam-bending (CBB) device: **a** one CBB device building unit oriented in the x–y plane and surrounded everywhere by a cladding block, **b** the structure and refractive-index (n) profile of one CBB device together with its input and output cores 'n = 1.4551', all enclosed within the cladding block material 'n = 1.45'. The CBB effective bending-radius (160 μm) is also illustrated. The reference axes of each tilted graded-index (TGI) waveguide (WG) is also indicated, **c** the electric-field magnitude 'a.u.' of 90° bended beam within one CBB device laying in the x–y plane. The locations of the first and second total-internal reflections (TIRs) within the first and second TGI-WG are indicated, respectively

2 Principle of operation

Figure 1a shows a simple 3D schematic diagram of one CBB building unit. It consists of one 90° CBB device with one input and one output core surrounded everywhere by a cladding region. The CBB device can be oriented in any direction within the 3D cladding space, and thus allowing for flexible designs.

Figure 1b shows the refractive index distributions of one CBB device together its input core, output core, and enclosing silica-glass cladding block. The cladding refractive index is 1.45 while the single-mode cores refractive indices are selected to be 1.5441 with a core diameter of 9 μm. The 90° CBB consists of two tilted graded-index (TGI) rectangular waveguides (WGs). Both WGs have 35 μm width and 9 μm height. While the first WG length is 120 μm and the second WG length is 130 μm. The effective total 90° bending-radius from input to output core is ≅ 160 μm. The graded index is selected to have a parabolic profile. The first WG (TGI #1) is tilted by $\theta_1 = 22.5°$ with respect to input core center-axis, while the second WG (TGI #2) is tilted by $\theta_2 = 67.5°$. The input core beam is launched almost at the center of TGI-WG #1 input, while the output core beam is collected almost at the center of TGI-WG #2 output.

The FDTD simulations (http://www.lumerical.com) are performed to validate the CBB device operation. Figure 1c shows the electric filed magnitude in arbitrary-units (a.u.) of propagating beam inside the CBB device. The beam is bended at 90° in two steps, each step is 45° through one TGI-WG. The input beam is guided through the graded-index WG #1 while preserving its confined beam shape to satisfy the wave-guiding condition until it experiences the first TIR (TIR-1) at the WG boundary. The confined beam deflects by twice the incidence angle on that interface boundary, because the reflection angle is equal to the incidence angle. Then, it continue as a confined beam to WG #1 output. Although the first TGI is tilted by 22.5°, its output beam is bended by a total angle of 2 × 22.5°= 45°. The same operating principle applies to the second TGI-WG. Which means the confined beam will further experience another 45° bending by TIR-2 to end up with a total bending angle of 90° at the second WG output core.

It is worth mentioning that the more tilting angles of WGs, the more bending-angles could be achieved for confined beams, which in turn can yield a smaller bending radius and thus an overall small area. However, the WG tilting angle is limited by the numerical-aperture (NA) (i.e. maximum acceptance angle) of GI profile. The input beam should fall within the acceptance angle cone at WG input, otherwise its power will be lost as radiation modes inside cladding. The numerical-aperture for GI waveguide can be expressed as $NA = n_c \sin\theta_a \cong n_o\, a\, \alpha$ (Saleh and Teich 2007). Where 'n_c' is the input core refractive index, 'θ_a' is the WG acceptance angle, 'n_o' is the GI peak value, 'α' is a coefficient that depends on parabolic GI slope, and 'a' is the effective GI half-width. Therefore, smaller bending radius could be achieved for higher values of 'n_o', 'α', and/or 'a'. For the case here, the selected values of these parameters are $n_c = 1.4551$, $n_o = 1.63$, $\alpha = 24.2684 \times 10^{-3}\ \mu m^{-1}$, and a ≅ 17 μm. Therefore, the maximum acceptance angle here is ≅ 27.53°. However, the tilting angle is selected to be a little bit less (i.e. 22.5°) in order to achieve a 45° bending after each WG stage with a total of 90° bending angle.

It is worth mentioning that Fig. 1c does not show a significant sign of radiation loss inside cladding region (e.g. beam power leakage), which indicates a very small bending-loss (i.e. insertion-loss) as will be discussed later. Also, the confined beam propagation ensures single-mode matching between input and output cores, and thus direct connection with standard optical fibers without a need for special mode tapers or spot-size converters.

Figure 2 shows the FDTD simulations of some different beam routing configurations using cascaded CBB devices. In Fig. 2a, an 180° beam-bending is realized in the x–y plane using two cascaded stages of 90° CBB devices. As shown, the input and output beams are in-parallel with horizontal separation in the x-direction of $\cong$ 380 μm. If the intermediate core length between the two CBB stages is adjusted, this separation can be controlled to be more or less according to the required design. However, the smallest separation should be twice the beam bending radius, i.e. $2 \times 160 = 320$ μm. In Fig. 2b, an S-shaped beam layout is presented in the x–z plane. Here, the output beam is displaced away from the input beam in the z-direction. It is worth mentioning that the input beam to the S-shape route could be coming from an output beam of another CBB device in the x–y plane, similar to that shown in Fig. 1c, and thus making 3D routing. Figure 2c shows a spiral beam propagation route in the x–z plane using 10 cascaded CBB devices. The spiral input at the center could be also a CBB device output in the y–z plane. The spiral here shows the ability to cascade several CBB devices and to maneuver in space within a small area of almost 0.6 mm $\times$ 0.6 mm $= 0.36$ mm^2. The accumulating insertion-loss due to the 10 cascaded devices will be discussed later.

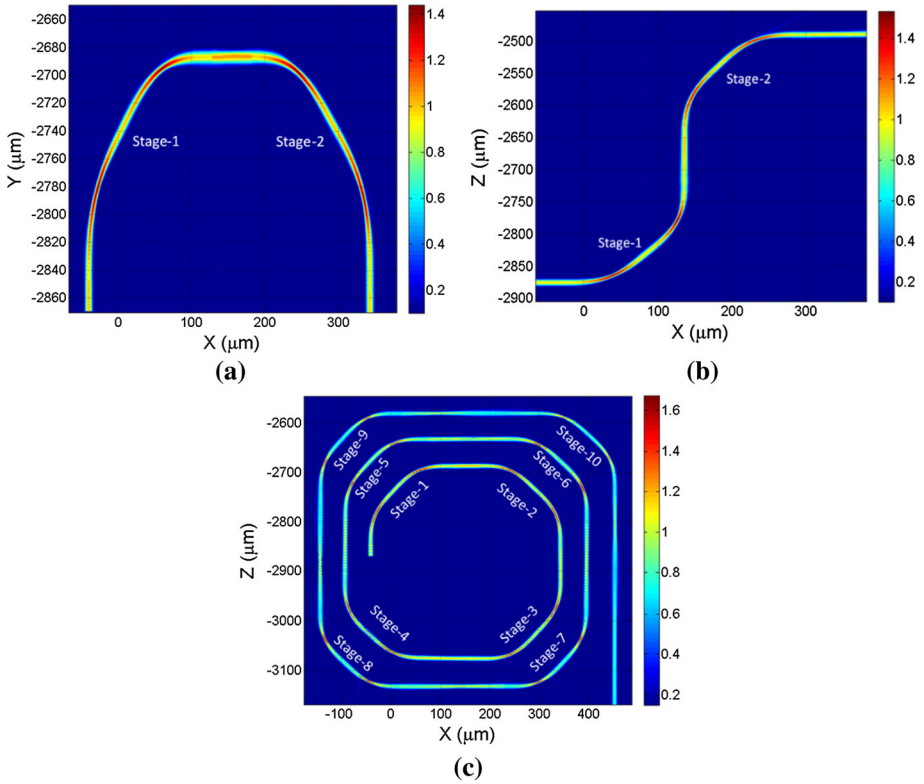

Fig. 2 The electric-field magnitudes 'a.u.' of different beam bending configurations using several cascaded CBB devices: **a** an 180° beam bending using two cascaded CBB stages in the x–y plane, **b** an S-shaped beam bending using two cascaded CBB devices in the x–z plane, **c** a spiral beam bending configuration using 10 cascaded stages of CBB devices in the x–z plane

2.1 Theoretical analysis

Besides FDTD simulations, the following is a theoretical analysis of CBB device that is carried out to illustrate and verify its principle of operation. A beam trajectory in the graded-index waveguides of CBB device can be expressed by the Eikonal differential equation (Saleh and Teich 2007):

$$\frac{d^2x}{dy^2} = \frac{1}{n(x)}\frac{dn(x)}{dx} \tag{1}$$

where the x–y coordinate reference axes are defined in Fig. 1b for the first and second TGI refractive indices. The parabolic graded index profile can be generally expressed as:

$$n(x) = n_o\left(1 - \frac{\alpha^2}{2}x^2\right) \tag{2}$$

where 'α' is a constant coefficient, and 'n_o' is the peak refractive-index. As stated above, $n_o = 1.63$ and $\alpha = 24.2684 \times 10^{-3}\ \mu m^{-1}$. The x–y dimensions here are measured in micrometers. By substituting Eq. (2) into Eq. (1) and solving for a beam trajectory inside the CBB waveguide, we can get the following two harmonic solutions that approximately describe the output beam position 'y_{out}' and angle 'θ_{out}' as a function of input beam position 'y_{in}' and angle 'θ_{in}':

$$x_{out} \cong (x_{in})Cos(\alpha y) + \frac{\theta_{in}}{\alpha}Sin(\alpha y) \tag{3}$$

$$\theta_{out} = \frac{dx_{out}}{dy} \cong -(y_{in})Sin(\alpha y) + \theta_{in}Cos(\alpha y) \tag{4}$$

The input (output) angle are usually measured between the beam propagation direction and the y-axis at the input (output) interface of each graded-index profile. The following Table 1 summarizes the theoretical results of this mathematical analysis by solving Eqs. (3) and (4).

Note that the difference in tilting angles between first and second TGIs is $67.5° - 22.5° = 45°$. Therefore, the input beam angle to TGI-WG #2 is $45° - 20.512° = 24.488°$. However, applying Snell's law (Saleh and Teich 2007) at the interface between the TGI-WG #1 with $n = 1.59$ and the TGI-WG #2 with $n = 1.63$, result in an input angle to second stage $\cong 23.849°$. By adding the tilting angle of the second stage to its output beam angle, we can get the total output beam bending angle $\cong 67.5° + 23.1° = 90.6°$. This approximate analysis shows a good agreement with the numerical simulations that is already shown in Fig. 1.

Table 1 The theoretical analysis results for beam trajectory in CBB device

Beam trajectory	TGI #1		TGI #2	
	Input	Output	Input	Output
y (μm)	1.5	5.28	0	− 4.34
θ (°)	22.5	− 20.512	23.849	− 23.1

3 Performance evaluation

The FDTD simulations are utilized to evaluate the CBB device performance from input to output fibers, over the S, C, L, U wavelength bands covering a wideband range starting from 1.46 μm up to 1.675 μm. The evaluated characteristic parameters are insertion-loss (IL), polarization-dependent loss (PDL), and return-loss (RL). All parameters are evaluated in 'dB'. The IL is calculated as 10Log_{10} (P_{out}/P_{in}), where P_{out} is the electric field power at device output, and P_{in} is the input source power. The PDL is calculated as the difference in insertion-loss between TM and TE polarizations. The RL is calculated as 10Log_{10} ($P_{reflect}/P_{in}$), where $P_{reflect}$ is the reflected electric field power at device input interface, and P_{in} is the input source power.

Figure 3a shows the CBB device insertion-loss over the S, C, L, U bands for both TM and TE polarizations. The IL is mostly due to bending-loss, in addition to some coupling loss. The overall IL is small with some variations over the entire wavelength range. The IL maximum magnitude is $\cong$ 0.24 dB for TE polarization at $\lambda = 1.471$ μm, while the minimum magnitude is $\cong$ 0.148 dB for TM polarization at $\lambda = 1.544$ μm.

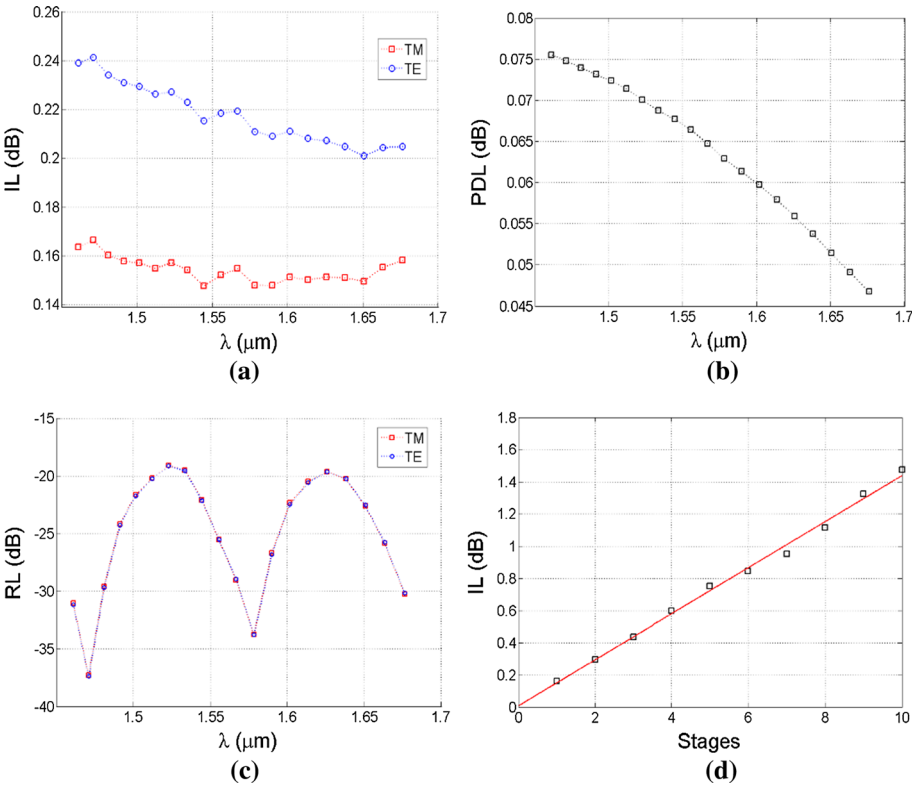

Fig. 3 The Performance evaluation of CBB device over the S, C, L, U wavelength bands: **a** the insertion-loss (IL) for both TM and TE polarizations, **b** the polarization-dependent loss (PDL) calculated as the difference in IL between TE and TM polarizations, **c** the return-loss (RL) calculated at input of CBB device for both TM and TE polarizations, **d** The recorded insertion-loss at each stage of spiral beam bending route (shown in Fig. 2c) together with the best-fitted straight-line between recorded points

Figure 3b shows the polarization-dependent loss of CBB device. The maximum PDL magnitude is 0.0755 dB at $\lambda = 1.461$ μm. Thus, the PDL can be considered negligible and thus the CBB device is polarization insensitive. It is worth mentioning that both IL and PDL indicate an excellent performance over the S, C, L, U wavelength bands.

Figure 3c shows the return-loss (RL) evaluated at the input of CBB device over the SCLU bands for both TM and TE polarizations. The RL is also polarization insensitive. It is mainly due to the difference between the refractive indices of cores and the device WGs. However, the RL fluctuates slowly over the entire wavelength range due to some Fabry–Perot effect or multiple reflections among the cores and TGI-WGs interfaces. The recorded RL at wavelength of 1.555 μm in the C-band is − 29 dB. The maximum RL is − 19 dB at $\lambda = 1.523$ μm, and the minimum RL is − 37 dB at $\lambda = 1.471$ μm.

Figure 3d shows the accumulating IL when cascading several stages of CBB devices as the case with the spiral route already illustrated in Fig. 2c. The IL is evaluated after each CBB stage at the operating wavelength of 1.555 μm with TM polarization. Then, the recorded IL values are best curve-fitted with a straight line. The IL increases when adding more stages with a slope equals to $\cong -0.14$ dB/stage. The slope is considered small, and it results in accumulating insertion-loss with a magnitude $\cong$ 1.47 dB after the 10th stage.

4 Universal multicore connector

In this section a simple UMC example is considered and evaluated using FDTD simulations. The universal multicore connector consists of a bulk cladding silica-glass material, which encloses a plurality of space-division multiplexed cores. The multicores can be designed to establish the desired connections between input and output cores of MCFs and/or SMFs. The UMC connections are merely established on a core-to-core basis. The basic building unit of UMC is the CBB device. The CBB can be oriented in any three dimension (3D) direction or cascaded in stages within cladding-block space to achieve different routing configurations between the input and output cores. The sharp bending allows maneuvering routes around small corners, and thus results in an overall small area. Besides, it gives flexibility in layout designs. Such characteristics make the device universal in a way that it can establish various connections among different types and structures of single-mode MCFs and/or SMFs.

Figure 4a, b show the UMC example. It connects and redistributes the cores of three different MCFs and two SMFs. The cladding boundaries of UMC and optical fibers are defined by white dashed lines. The specifications of optical fibers connected to UMC different ports (P1 to P10) are as follows. MCF-1 (Fig. 4c) has 3-cores with core-separation of 40 μm. MCF-2 (Fig. 4d) has 3-cores with core-separation of 25 μm. MCF-3 (Fig. 4d) has 2-cores with core separation of 40 μm. SMF-1 and SMF-2, have single cores and are connected to UMC ports P9 and P10, respectively. All fibers have cores with diameter of 9 μm and refractive-index of 1.4551, while their claddings have diameters of 125 μm with a refractive-index of 1.45. The simulated electric field magnitudes show the propagation routes among UMC ports. Figure 4a shows an upper cross-section of UMC routes which includes MCF1 ports P1, P2 and MCF2 ports P5, P6. While Fig. 4b shows a lower cross-section of UMC route which includes MCF1 port P3 and MCF2 ports P4. In Fig. 4a, the signal coming out of port-1 for MCF-1 is bended by 180° and routed back to SMF-2. Which is considered a loopback connection that could be useful in some applications such as optical sensing or measurements and diagnosing of optical fiber

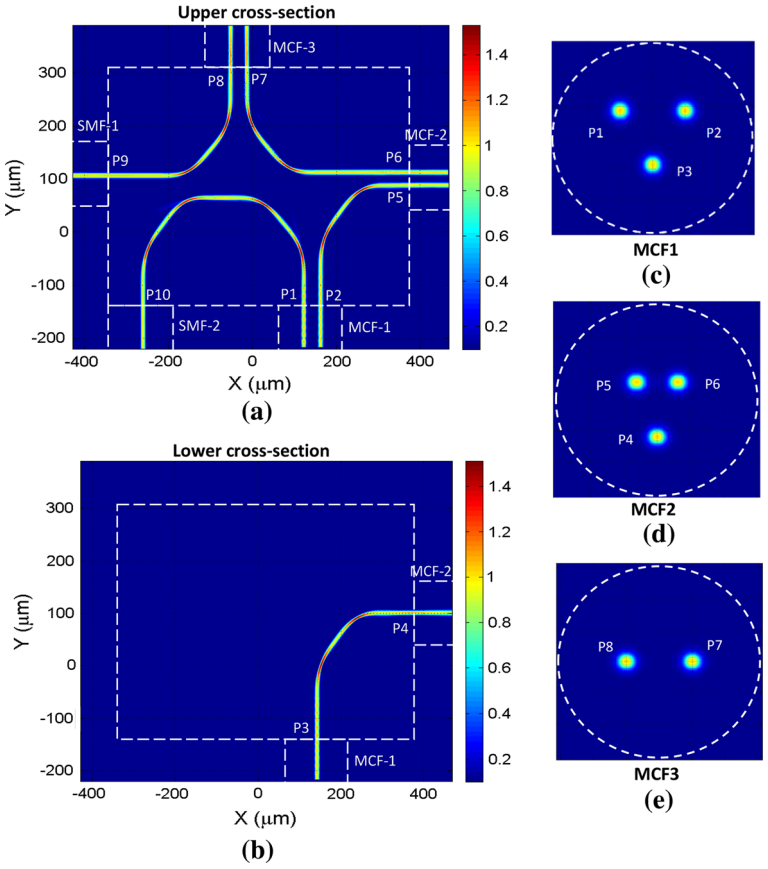

Fig. 4 A simple example of UMC configuration with 10-ports connected to three different MCFs and two SMFs. It shows the electric-field magnitudes 'a.u.' of redistributed propagating signals through different cores. The white dashed lines indicate the boundaries of both UMC and optical fibers cladding regions: **a** An upper cross-section of UMC including MCF1 ports P1, P2 and MCF2 ports P5, P6, **b** A lower cross-section through UMC including MCF1 port P3 and MCF2 port P4, **c** the cross-section of 3-cores MCF1 at UMC ports P1, P2, P3 with 40 μm cores-separation, **d** the cross-section of 3-cores MCF2 at UMC ports P4, P5, P6 with 25 and 40 μm cores-separations, **e** the cross-section of 2-cores MCF3 at UMC ports P7, P8 with 40 μm cores-separation

transmission links. The cores of MCF-2 are redistributed between MCF-1 and MCF-3 which already have different core separations. Another core of MCF-3 is connected to SMF-1 which could be used for adding or dropping core signals at some fixed node location. Note that all such bendings and redistributions of beams are done in a small device area of almost 0.5 mm × 0.5 mm = 0.25 mm^2. Of course, this example can be extended to connect a single MCF to several SMFs which could be useful at the transmitters and/or receivers ends.

The MCF-2 in this example is chosen to have a 25 μm core separation in order to check for the worst-case bending cross-talk (XT), when the CBB devices are placed very close to each other. Figure 5 shows the measured cross-talk when a source is connected to one UMC port and the bending XT leakage signals are measured at other remaining eight ports, of course, excluding the transmission port. The XT is calculated as 10Log_{10} ($P_{leakage}/P_{in}$),

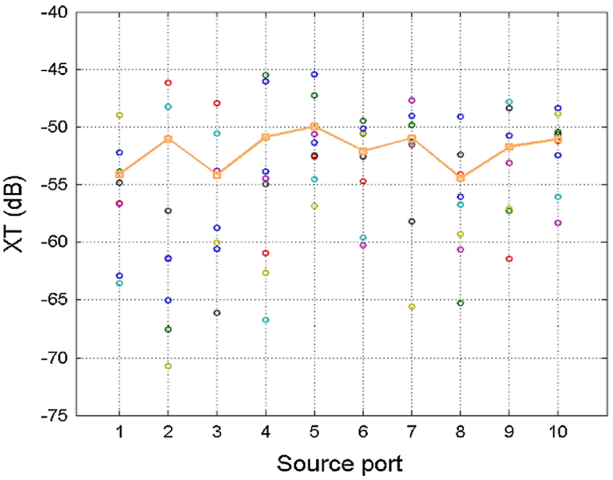

Fig. 5 The estimated crosstalk (XT) collected at the 8-ports of UMC when an input signal is injected at one single source-port. The solid curve is the average XT recorded at each port

where $P_{leackage}$ is the leaking electric field power at one device port, and P_{in} is the input source power. As shown in Fig. 5, the maximum value of XT does not exceeds − 45 dB in the worst-case, however it could be as low as − 70 dB at some other ports. The average XT calculated for all ports are showed by the solid-line curve. It indicates a maximum average XT of − 50 dB. Which is considered a very good performance.

5 Tolerance to core variations of MCFs

In addition to different cores separations and arrangements in single-mode MCFs that are discussed above, some other MCFs variations such as cores diameters and refractive-indices are explored in this section to verify the universality of UMC with different types of MCFs.

First, the MCF core diameter is considered. The maximum core diameter should not exceed $\Phi = 9.78$ μm to maintain a single-mode operation. Figure 6a shows the changes in IL for $\Delta\Phi = \pm 0.78$ μm over the entire SCLU wavelength range. As shown, the worst-case IL magnitude is 0.172 dB which is still very small.

Second, the MCF core refractive index is considered. The core maximum normalized refractive-index difference (Δ) should not exceed $\Delta = 0.43\%$ to maintain a single-mode operation. Figure 6b shows the changes in IL for $\Delta = 0.27\%$ up to 0.43% over the entire SCLU wavelength range. As shown, the worst-case IL magnitude is almost 0.21 dB which is still reasonable.

Therefore, the UMC can be considered a universal device in a sense that it can match various types of single-mode MCFs which have different designs for core arrangements, separations, diameters, and refractive indices. This is in addition to UMC flexibility in design and its small size area.

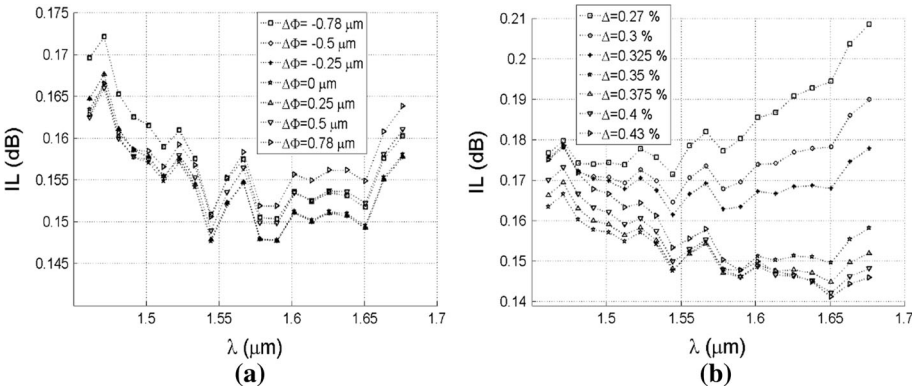

Fig. 6 The performance tolerance to variations in MCFs cores diameters and refractive indices over the S, C, L, U wavelength bands: **a** the insertion-loss as a function of change in MCF core-diameter (ΔΦ), **b** the insertion-loss as a function of change in MCF core normalized refractive-index difference (Δ%)

6 Tolerance to design parameters variations

The tolerances of CBB performance to variations in some of its critical design parameters are investigated in this section. These tolerances could be used to set the margins for device fabrication sensitivity errors. In other words, having large design parameters tolerances, relaxes the constraints on device fabrication errors and in turn it can facilitate its fabrication. The key performance indicator or figure of merit here would be the CBB device insertion-loss.

Figure 7a shows the device IL tolerance to variations in waveguides widths (Δw) over the entire SCLU wavelength range. For $\Delta w = 5$ to -5 μm, the IL remains within the range of 0.13–0.26 dB, respectively. Which indicates a reasonable ± 5 μm margin that can tolerate errors in waveguides widths. The highest margin limit is set to be $\Delta w = 5$, because at this value the minimum possible silica-glass refractive index ($n = 1.44$) is reached at the waveguides boundaries. By reducing the waveguide width further, $\Delta w = -6$ and -7 μm, The IL increases but still remains less than 1 dB. However beyond $\Delta w = -7$ μm, the IL exceeds 1 dB.

Figure 7b shows the device IL tolerance to variations in waveguides parabolic refractive-index coefficient (α) over the entire SCLU wavelength range. Where 'α' is mainly responsible for GI index profile slope. The maximum chosen value of 'α' is equal to 25.7×10^{-3} μm^{-1} to ensure the minimum silica-glass refractive not less than 1.44. While the minimum chosen value of 'α' is equal to 21.6×10^{-3} μm^{-1}, where the IL starts to exceed 1 dB for some certain wavelengths. Thus, for variation range of $\Delta\alpha \cong 4 \times 10^{-3}$ μm^{-1}, the IL remains below 1 dB. That range is considered reasonable for a good performance of CBB device.

Figure 7c, d show the tolerance of device IL to input and output cores misalignments, respectively. The 'Δx' and 'Δy' represent the offset in 'x' and 'y' directions, respectively, with respect to the best alignment position (i.e. alignment for minimum IL). As shown in Fig. 7c, the input core misalignment can range from -6 to 8 μm, whereas the additional IL remains below 1 dB. While in Fig. 7d, the output core misalignment can range from -4 to 8 μm, whereas the additional IL remains below 1 dB. Both alignment mismatch

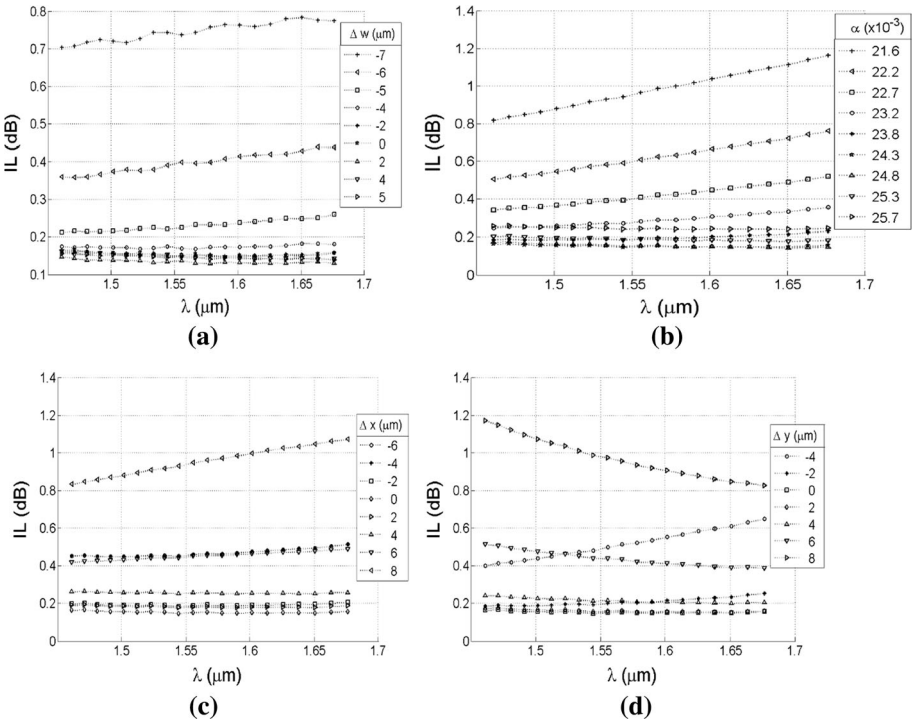

Fig. 7 The performance tolerance to variations in CBB design parameters over the S, C, L, U wavelength bands: **a** the insertion-loss as a function of change in GI waveguide widths (Δw), **b** the insertion-loss as a function of change in waveguide GI coefficient 'α' (μm^{-1}), **c** the insertion-loss as a function of input core misalignment (Δx), **d** the insertion-loss as a function of output core misalignment (Δy)

ranges indicate good margins for alignment errors without significant degradations in device performance.

Finally, although the scope of this work is numerical demonstration of CBB and UMC devices, it is worth to comment on the feasibility of devices fabrication. The key issue in fabrication is to realize the graded-index profiles of CBB as shown in Fig. 1b. One suggested fabrication technique is flame hydrolysis deposition (FHD) (Takahashi 2003; Kawachi 1990). It is a simple method that can give a high precision and excellent reproducibility of graded-index profiles. The FHD deposits particles of silica-glass material point-by-point using a scanning flame torch. The torch has controllable raw material vapor composition and flow rate, both could be used to adjust refractive indices profiles and thickness of each deposited layer (Yanagawa et al. 1992). Therefore, FHD technique can be used to deposit silica-glass material of CBB device layer-by-layer in the x–y plane while moving along the z-direction. Within each layer, the flame gases compositions (i.e. mixing-ratios) and flow-rates can be pre-programed and modulated to achieve the desired graded or step refractive index distribution that spans each layer. By moving from one layer to another along the z-direction, the device entire block including its surrounding cladding could be written. The refractive index changes within each layer and between different layers could be used to define the WGs boundaries and dimensions, whether these WGs lay down within one layer or spans out of plane through multi-layers. Thus, this technique

could also be utilized to realize various UMC beam routing configurations comprising multiple CBB devices with different orientations.

7 Conclusions

A novel 90° CBB device with small bending-radius of 160 μm has been numerically demonstrated. The operating principle of CBB device is verified using both FDTD simulations and mathematical analysis. The device consists of two cascaded waveguides stages with tilted parabolic refractive-index profiles. The confined beam propagation inside WGs ensures single-mode beam-profile matching between input and output cores and direct connection with standard optical fibers without a need for special mode tapers or spot-size converters. The CBB device is the basic building block of UMC. The UMC can directly connect on a core-to-core basis between different types of standard single-mode MCFs and/or SMFs. The sharp bending of CBB inside UMC allows for adaptive and flexible core layout connections, in addition to maneuvering around small corners in order to get overall small area. Testing by FDTD simulations over wide wavelength range of S, C, L, and U bands shows small device insertion-loss and polarization-dependent loss with reasonable return-loss and crosstalk. It also shows cascadability and good tolerance to variations in MCF cores diameters and refractive indices, in addition to variations in CBB device design parameters.

Acknowledgement The author gratefully acknowledge the technical and financial support from the Research Center at College of Engineering, and the Deanship of Scientific Research at King Saud University.

Funding This research did not receive any specific grant from funding agencies in the public, commercial, or not-for-profit sectors.

References

Awad, E.: Multicore optical fiber Y-splitter. Opt. Express **23**, 25661–25674 (2015a)

Awad, E.: Data interchange across cores of multi-core optical fibers. Opt. Fiber Technol. J. **26**(B), 157–162 (2015b)

Chralyvy, A.: Plenary paper: the coming capacity crunch. In: Proceedings of the 35th European conference on optical communication, Vienna, Austria. Publisher, IEEE, pp. 1–1 (2009)

Essiambre, R., Kramer, G., Winzer, P., Foschini, G., Goebel, B.: Capacity limits of optical fiber networks. J. Lightwave Technol. **28**(4), 662–701 (2010)

Essiambre, R.J., Ryf, R., Fontaine, N.K., Randel, S.: Breakthroughs in photonics 2012: space-division multiplexing in multimode and multicore fibers for high-capacity optical communication. IEEE Photonics J. **5**(2), 0701307 (2013). https://doi.org/10.1109/JPHOT.2013.2253091

Kaminow, I., Li, T., Willner, A.: Optical Fiber Telecommunications: Systems and Networks. Chap. 1, vol. 6B, p. 13. Academic Press Elsevier, Cambridge (2013)

Kawachi, M.: Silica waveguides on silicon and their application to integrated-optic components. Opt. Quantum Electron. **22**(5), 391–416 (1990)

Klaus, W., Sakaguchi, J., Puttnam, B.J., Awaji, Y., Wada, N., Kobayashi, T., Watanabe, M.: Free-space coupling optics for multicore fibers. IEEE Photonic Technol. L. **24**(21), 1902–1905 (2012)

Leon-Saval, S.G., Argyros, A., Bland-Hawthorn, J.: Photonic lanterns: a study of light propagation in multimode to single-mode converters. Opt. Express **18**(8), 8430–8439 (2010)

Li, Y., Tong, L.: Mach-Zehnder interferometers assembled with optical microfibers or nano-fibers. Opt. Lett. **33**(4), 303–305 (2008)

Lumerical solutions. http://www.lumerical.com. Accessed 2016

Popovic, M., Wada, K., Akiyama, S., Haus, H.A., Michel, J.: Air trenches for sharp silica waveguide bends. J. Lightwave Technol. **20**(9), 1762–1772 (2002)

Richardson, D., Fini, J., Nelson, L.: Space-division multiplexing in optical fibres. Nat. Photonics **7**(5), 354–362 (2013)

Saleh, B.E.A., Teich, M.C.: Fundamentals of Photonics, Chap. 1, 2nd edn. Wiley, New York, pp. 5–24 (2007)

Takahashi, H.: Planar lightwave circuit devices for optical communication: present and future. Proc. SPIE **5246**, 520–531 (2003)

Thomson, R., Bookey, H., Psaila, N., Fender, A., Campbell, S., MacPherson, W., Barton, J., Reid, D., Kar, A.: Ultrafast-laser inscription of a three dimensional fan-out device for multicore fiber coupling applications. Opt. Express **15**(18), 11691–11697 (2007)

Thomson, R., Harris, R., Birks, T., Brown, G., Allington-Smith, J., Bland-Hawthorn, J.: Ultrafast laser inscription of a 121-waveguide fan-out for astrophotonics. Opt. Lett. **37**, 2331–2333 (2012)

Wijeratne, I.N.M., Kejalakshmy, N., Agrawal, A., Rahman, B.M.A., Grattan, K.T.V.: Numerical analysis of second harmonic generation in soft glass equiangular spiral photonic crystal fibers. IEEE Photonics J. **4**(2), 357–368 (2012)

Yanagawa, H., Shimizu, T., Nakamura, S., Ohyama, I.: Index-and-dimensional taper and its application to photonic devices". J. Lightwave Technol. **10**(5), 587–592 (1992)

Zhu, B., Taunay, T.F., Yan, M.F., Fini, J.M., Fishteyn, M., Monberg, E.M., Dimarcello, F.V.: Seven-core multicore fiber transmissions for passive optical network. Opt. Express **18**(11), 11117–11122 (2010)

Zhu, B., Fini, J., Yan, M., Liu, X., Chandrasekhar, S., Taunay, T., Fishteyn, M., Monberg, E., Dimarcello, F.: High-capacity space-division-multiplexed DWDM transmissions using multicore fiber. J. Lightwave Technol. **30**(4), 486–492 (2012)